Voltage Modulated Untwist Deformations and Multispectral Optical Effects from Ion Intercalation into Chiral Ceramic Nanoparticles

Xiao Shao,[1,2,3] Cheng Zhu,[4] Prashant Kumar,[1,2] Yanan Wang,[1,2] Jun Lu,[1,2] Minjeong Cha,[2,5] Lin Yao,[1,2] Yuan Cao,[1,2] Xiaoming Mao,[5] Hendrik Heinz,[4]* Nicholas A. Kotov, [1,2,6]*

[1]Department of Chemical Engineering, University of Michigan, Ann Arbor, MI, 48109, USA;

[2]Biointerfaces Institute, University of Michigan, Ann Arbor, MI, 48109, USA;

[3]Tianjin Key Laboratory of Applied Catalysis Science and Technology, School of Chemical Engineering and Technology, Tianjin University, Tianjin 300354, China;

[4]Department of Chemical and Biological Engineering, University of Colorado at Boulder, Boulder, CO, 80309, USA;

[5]Department of Physics, University of Michigan, Ann Arbor, MI, 48109, USA;

[6]Department of Materials Science and Engineering, University of Michigan, Ann Arbor, MI, 48109, USA;

*Corresponding author. Email: hendrik.heinz@colorado.edu, kotov@umich.edu

Abstract: Geometric reconfiguration of chiral ceramic nanostructures after ion intercalation should favor specific nanoscale twists that should lead to unusually strong chiroptical effects. Based on multifaceted experimental, simulation, and theoretical data, here we show that V_2O_3 nanoparticles have 'built-in' chiral distortions caused by multipoint binding of enantiomers of tartaric acid to the surface of inorganic core. As evidenced by spectroscopy/microscopy techniques and calculations of nanoscale chirality measures, the intercalation of Zn^{2+} ions into the V_2O_3 lattice results in particle expansion, untwist deformations and related decrease of chirality. Coherent deformations in the particle ensemble manifest as changes in sign and positions of multiple circular polarization bands at ultraviolet, visible, mid-, near- (NIR) and infrared (IR) wavelengths originating in the electronic states of the surface ligands and the semiconductor cores. The g-factors observed for IR and NIR spectral diapasons are ~100-400 times higher than those for previously reported dielectric, semiconductor and plasmonic nanoparticles. Nanocomposite films layer-by-layer assembled (LBL) from V_2O_3 nanoparticles reveal cyclic voltage-driven modulation of optical activity. Device prototypes for IR and NIR range problematic for liquid crystals and other organic materials, were demonstrated. High optical activity, synthetic simplicity, sustainable processability and environmental robustness of the chiral LBL nanocomposites provide a versatile platform for photonic devices. Similar reconfigurations of particle shapes are expected for multiple chiral ceramic nanostructures with a variety of optical, electrical, and magnetic properties.

Reversible incorporation of metal ions into ceramic materials, such as silicon, cobalt oxide, and nickel oxide, is well known in energy storage devices and causes strong distortions of their crystal lattices. At the particle level, the relations between the atomic or nanometer scale structure of the particles and the direction of exerted stress are largely unpredictable, being strongly affected by random geometric features and particle defects [1]. We noted that the many ceramic materials, exemplified by Co_3O_4 and NiO, can produce chiral nanoparticles (NPs) with strong polarization rotation [2]. In these and other cases of chiral nanostructures, for instance from gold [3] and mercury sulfide [4], the strong optical activity originates from the chiral bias that enantiomeric organic ligands on particle surfaces exert on the crystal lattice. Since the chirality and twisting deformations are intrinsically related, as can be seen in chiral origami, kirigami, and metamaterials [5–8], one could expect that nanoscale chirality will define deformation patterns upon ion intercalation into nanostructures. The resulting chiral deformations of particle lattices and shapes occurring coherently over the entire ensemble of NPs with the same handedness must inevitably lead to strong optical polarization effects that can be of interest for rapidly growing family of devices for chiral photonics [2,7,9,10], sensors [11], and displays [12].

To test this hypothesis, we synthesized NPs of vanadium sesquioxide, V_2O_3, by controlled hydrolysis of vanadium (III) chloride in the presence of (*R,R*) and (*S,S*) tartaric acid (TA), also known as *L*- and *D*-TA (Methods and Supporting Information, SI); the resulting V_2O_3 particles will be correspondingly referred to as *L*- or *D*-NPs and racemic (*rac-*) NPs when an equimolar mixture of TA enantiomers was used. The choice of V_2O_3 was governed by its small band gap of $E_g = 0.3$ eV compared to E_g for other metal oxides (Table

S1), which makes nanoscale V_2O_3 suitable for engineering of devices in visible and infrared parts of the spectrum facilitated by its electrochromic and magnetic properties [13–15].

Chemical Structure of Chiral V_2O_3 NPs. The atomic composition and structure of the prepared V_2O_3 NPs was established based on electron microscopy and vibrational spectroscopies. Transmission electron microscopy (TEM) showed that size of *L*-NPs was 2.31 ± 0.06, 2.41 ± 0.07, and 2.54 ± 0.02 nm when synthesized at pH 3, 7, and 11, respectively (**Fig. 1A-F** and Fig. S3). Small size of chiral particles is essential in order to minimize the solid-state diffusion time required for ion intercalation.

Scanning transmission electron microscopy (STEM), energy-dispersive spectral (STEM-EDS) mapping confirmed that the NP composition was consistent with vanadium oxide for all pH values (Fig. S3). The position of the vanadium $2p$ peak in the X-ray photoelectron spectroscopy (XPS) shows that vanadium atoms are in the +3 state (Fig. S4). Crystalline domains with lattice spacing of ~0.21 nm is consistent with the (610) planes of monoclinic V_2O_3; they were always observed in the central part of the NPs but the crystallinity of V_2O_3 was visibly reduced at the interface where strong distortions may occur (**Fig. 1A-C**).

The chemical structure of the NPs obtained at different values of pH was subsequently assessed by multiple modalities of vibrational spectroscopies. The strong bands at 878, 879, and 944 cm^{-1} in the Raman scattering spectra (**Fig. 1G**, S5) of NPs originate from V=O bonds. Being strongly dependent on pH, they are situated on the NP surface, and are consistent with V^{3+} sites interacting with TA ligands. The typical binding conformations and number of coordination bonds of the TA species (H_2T, HT^-, and T^{2-}) on V_2O_3 NPs. The bands

at ~532 and ~629 cm^{-1} originate from the stretching vibration modes of V−O and V−O−V bonds, respectively, of the monoclinic V_2O_3 lattice and only appear for the NPs at pH 3 and 7. However, in the V_2O_3 NPs synthesized at pH 11 that have the thickest amorphous layer, these Raman peaks disappear. The broadened bands located at 246 and 367 cm^{-1} are assigned to the bending vibration of the V−O bonds [16] in the NP interior and the interface. The Raman optical activity (ROA) spectra display a band below 600 cm^{-1} (Fig. S6), which corresponds to solid state phonons. [17] The short range and heterogeneity of the V_2O_3 core results in broadening. However, one can simultaneously see that the chiral distortions of the inorganic phase results in their chirality as well [2].

The complementary Fourier transformation infrared (FTIR) spectra show distinct shifts of the peaks associated with −OH, C=O, and C−O vibrations in TA moieties after binding to NPs (**Fig. 1H**, S7), which are consistent with the coordination bonding between oxygen atoms of the hydroxy/carboxyl groups of TA and V^{3+} sites on the NP surface. The bands at 1550-1650 cm^{-1} are associated with amide-II vibration modes of TA-V_2O_3, while the peak at 1065 cm^{-1} corresponds to the stretching vibration of the V=O bond in the interior of NPs [16].

To better understand the coordination of TA to V_2O_3 NPs and, thus, the structural changes upon Zn^{2+} intercalation, we performed molecular dynamic (MD) simulations using the Interface Force Field (Table S2), which is capable of accurate description of nanometer scale particles of complex oxides [18]. Three atomistic models of NPs utilized for pH of 3, 7, and 11 incorporate previously reported surface chemistry (**Fig. 2A, B**, S8, S9A-C), and computed binding data are consistent with TEM, XRD, Raman, and FTIR data described

above. The MD models were additionally validated by the calculation of radial distribution functions (RDF) and vibrational circular dichroism (VCD) spectra (Fig. S10C-I). The pH-dependent RDF peaks show that COO^- groups had the strongest and closest bonding with the NPs (Fig. S10C). The calculated VCD spectra (Fig. S10G-I) matched the experimental ones, which is quite remarkable considering their complexity and demonstrates the accuracy of the atomistic models over nanosecond dynamics.

Both vibrational spectroscopies and MD data revealed that TA forms strong vanadium-oxygen coordination bonds with NP surfaces (**Fig. 2A**, and Fig. S10B). In addition to single bonding sites, the MD trajectories show single TA molecules attaching to V_2O_3 surfaces with two, three, and even four coordination bonds. The multi-prong, or 'staple' configurations of surface ligands [19,20] are likely to form via collective binding of neighbor and next-nearest neighbor carboxyl groups to the NP surface (Fig. S10B and Table S3).

The MD data also pinpoint the nature of the chirality transfer from the ligands to NPs. The tight binding of TA strains the crystal lattice of V_2O_3, which results in chiral distortions of the latter with the interfacial layer of the NPs being the most affected. The surface maps of volumetric strain show that the magnitude of the strain increases with pH due to stronger binding of TA ligands (**Fig. 2C**, and Fig. S11). The consequence of the strain is the presence of chiral structural features and namely the distorted interfacial layer, which is clearly visible in STEM images (**Fig. 1F**). The twisting deformations at the TA binding sites can also be recognized as a change of local geometry for V_2O_3. Compared with the ligand-free NPs (21.8°), the dihedral angle calculated for *L*-NPs became larger (31.6°), while that for *D*-NPs

decreased to 5.1° (Fig. S12), indicating that the strain and distortions are chiral and differ in directions for *L*- and *D*-TA.

The chirality transfer from the TA ligands to the inorganic core can be rigorously evaluated using weighted Osipov-Pickup-Dunmur chirality measure (wOPD) [21]. The atomistic models of particles without TAs on their surfaces at all pH conditions were achiral and revealed wOPD ≈ 0. The same NPs equilibrated with *L*- or *D*-TA displayed negative and positive wOPD that sharply increases in absolute values for pH 11 to -4.8 and +10.5 for *L*- or *D*-NP, respectively (**Fig. 2D).** its sharp increase with pH points to the chirality transfer via lattice distortions due to TA binding to NP surface because the rise of wOPD parallels the increase of surface strain (**Fig. 2C**). We note despite limitations of wOPD being elaborated in the past [22], the geometrical reconfigations restricted to the twist-unwist deformations reveal chirality continuum and inevitably pass through the zero chirality state when changing the sign from positive to negative [23].

Optical Properties. The mirror asymmetry of the NPs ought to translate into their optical activity. Indeed, circular dichroism (CD) spectra of *L*- and *D*-NPs display multiple positive and negative peaks from UV to IR parts of the spectrum (**Fig. 3C, D**, S13A, B). The negative CD peak of unbound *L*-TA typically observed at 210 nm, splits into three peaks with two new peaks at 185 and 240 nm (Fig. S13C, D), due to strong coordination to the surface in different 'staple' configurations. The NIR band between 700 and 1200 nm originates from the V_2O_3 polaronic states, which are strongly coupled to lattice distortions and surface states as was identified previously for vanadium oxides [13], WO_3 NPs [24] and other metal oxides [25]. The CD

spectrum disappears in *rac*-NPs while the UV-vis absorption spectrum is the same for *L*-, *rac-,* and *D*-NPs (Fig. S13E). The peaks in the UV part of the spectrum originate from the TA surface ligands. Distinct chiroptical activity, albeit less intense than for TA, was also observed in V_2O_3 NPs capped with *L*- and *D*-malic acid (MA) or *L*- and *D*-penicillamine (Pen) indicating the generality of the chirality transfer from chiral molecules on the surface to V_2O_3 NPs (Fig. S14-S16).

The position and intensity of the peaks in CD and absorption spectra were strongly dependent on pH varying progressively from 2 to 12 (**Fig. 3B-F**, S13A, B**)**. New CD bands of different signs emerge as pH changes reflecting the progression of interfacial binding of TA **(Fig. 3C, D)**. The prominent NIR band exhibited a strong blue-shift from 923 to 758 nm for *L*-NPs and from 921 nm to 841 nm for *D*-NPs with pH changing from 11 to 3 (**Fig. 3E**), which is associated with the strain-related changes in the energy of the polaronic state [13].

Optical asymmetry *g*-factors must exceed 0.05 for materials to be suitable for optical devices. Combining small size of the NPs and high *g*-factor represents a material engineering challenge specific for optically active nanostructures suitable for effective ion intercalation. The maximum *g*-factor of the NPs in the visible range is 0.086 at 654 nm, while that for the near-infrared (NIR) region is 0.079 at 1244 nm (Fig. S17, Tables S4 and S5). Considering the NPs in the same size regime of several nanometers in diameter (Table S6) [26], these *g*-factors are ~100 times higher than those for NPs from nonmetals and some plasmonic metals (Table S6) [9,27,28] and are ~400 times higher than that for the polaronic band of chiral WO_3 NPs [24].

As expected from the *g*-factor values, the strong polarization rotation was observed both for visible and NIR parts of the spectrum in the cross-polarizer optical system. The color of *L*-NPs dispersions continuously changed from red to purple by clockwise rotation of the post-cell polarizer **(Fig. 3G-H)**. *D*-NPs exhibit identical colors for a counterclockwise rotation. The red/green/blue/purple color palette corresponds to the peaks of 655/502/450/402 nm in the *g*-factor spectra (Fig. S17J) that play the dominant role in the transmitted light. Similar polarization rotation was observed for the cross-polarizer set-up based on a NIR camera **(Fig. 3I-K**, S18).

Ion intercalation into chiral nanoparticles. The rows of vacancies between V−O in monoclinic V_2O_3 can potentially accommodate other metal ions by formation of Frenkel defects due to Zn^{2+} substitutions of V^{3+} inside the NP core and creation of oxygen vacancies. Since the lattice spacing of V_2O_3 NPs is 0.1~0.37 nm, we chose the Zn^{2+} ion for intercalation because its diameter is 0.148 nm [14,29]. The successful incorporation of Zn^{2+} by adding 1 mL 2M $ZnSO_4$ solution to the 10 mL aqueous dispersions of V_2O_3 NPs, is demonstrated by the strong Zn peak in EDS mapping (Fig. S19 E, I, M). HRTEM images show that the lattice spacing for (610) planes of V_2O_3 expanded from ~0.2 to ~0.3 nm after Zn^{2+} ion intercalation (Fig. S19 G, H, K, L). Correspondingly, two new peaks ($2\theta = 16°$ and 24°) appeared in XRD (Fig. S20A) after Zn^{2+} intercalation in V_2O_3 NPs, which was also confirmed by FTIR. The mid-IR peak at 1620 cm^{-1}, corresponding to amide-II vibration modes of TA, gradually weakened and the peaks at 1115 cm^{-1} and 1055 cm^{-1}, corresponding to stretching vibration of the V=O bonds in the NP interiors became stronger (Fig. S20B). Raman scattering peaks describing the stretching mode of V=O groups on the NP surface shifted from 944 to 843 cm^{-}

[1] (Fig. S20C) after *L*-NPs were intercalated with Zn^{2+} ions. These experimental data showed weakening interactions between TA and the NP interface, overall lattice expansion, and new diffraction peaks that were also confirmed by MD simulations (**Fig. 2B** and Fig. S21A-C). Two XRD peaks in V_2O_3 NPs synthesized at pH 3 and 50°C were attributed to [211] and [51-2] planes in accord with 39-0774 standard XRD pattern (Fig. S22A).

After Zn-intercalation, the XRD peak from [51-2] lattice plane shifts as the consequence of the lattice expansion. The new peak appeared at $2\theta = 55^{\circ}$, which is in agreement with the simulation of XRD pattern from *L*-NPs after Zn-intercalation (Fig. S21B) and previous studies by Zhan et al [29]. Electron diffractions of *L*-NPs from the [41-1] crystal planes of monoclinic V_2O_3 with standard lattice spacing ~2.7 Å, also indicates the lattice expansion after Zn-intercalation and thus untwist deformation (Fig. S22B-D).

Concomitant changes in optical activity were observed. The CD intensity of Zn *L*-V_2O_3 NPs decreased across all bands from UV to NIR (Fig. S20D-I) and for NPs. The universal reduction of chiroptical activity upon ion-intercalation is related to coherent chirality-determined deformation of NPs due to expansion of the pre-twisted crystal lattice. Such deformations can be characterized by the geometrical models in **Fig. 2E** where layer expansion competes with chiral strain, leading to the twist-untwist mechanism which tunes chirality. As the chiral particle expands, it untwists, leading to the reduction of chirality. After ion intercalation, wOPD of NPs dropped from high absolute values to near 0 values (**Fig. 2D**), which confirms chirality reduction.

Voltage-driven optically active films from V$_2$O$_3$ nanoparticles. Modulated polarization rotation have been accomplished by mechanical deformations [6,30,31], magnetic field modulation 2, temperature variations [9,32], and changes in media chemistry [33]. The most technologically attractive processes are voltage-driven, which becomes possible due to polarization rotation upon ion intercalation in small chiral NPs. Compared to batteries, such electroactive films must also be transparent, which imposes stringent requirements on the NP size and their organization on the electrode. We engineered the films from V$_2$O$_3$ NPs addressing these requirements using layer-by-layer (LBL) deposition [34,35] by sequential immersion of ITO-glass substrates into 0.5% w/v poly(diallyldimethylammonium chloride) (PDDA) and 1% w/v polyacrylic acid (PAA)/V$_2$O$_3$. The advantage of LBL deposition over other methods of film preparation is the uniformity combined with high conductivity and transparency. A total of $n = 20$ PDDA/V$_2$O$_3$ multilayers were deposited (Fig. S23A, B) with optical density of ~0.5 D, 120-130 mdeg CD amplitude and g-factor of ~0.01 for the peak at 852 nm (**Fig. 4A, B**). Structural analysis of the L-TA films carried out by XPS and XRD (**Fig. 4C, D,** S24) showed that they are chemically similar to L-NPs. NIR absorption bands between 700 and 1200 nm (**Fig. 4B**) elevate their technological importance because it is difficult to realize chiroptical devices using voltage-driven transitions in liquid crystals.

Based on cyclic voltammetry (CV) data (Fig. S25A), for the intercalation of Zn^{2+}, there is no noticeable change after 60 cycles in the CV curves resulting in cyclic insertion and extraction of Zn^{2+} ions into the NP films (Fig. S25B). Transitioning from electrochemical to optical cells, we applied 1.0 V and 1.8 V to the NP films to investigate changes in optical

activity across UV-Vis-NIR regions upon cyclic ion intercalation and deintercalation (Fig. S26). The CD amplitude significantly decreases after Zn^{2+} ions intercalate into L- or D-V_2O_3 film (green line, Fig. S26A, B), which matched the experimental and theoretical data and indicated chirality reduction upon untwisting deformation associated with this process (**Fig. 2D, E**). The repeated cycling of Zn^{2+} intercalation and deintercalation of the L- and D-V_2O_3 films led to a periodic increase and decrease of CD intensity and the cyclic alternation of colors observed through cross-polarizers (**Fig. 4E-G**).

The recovery of optical activity after each cycle, however, was not complete (Fig. S26E, F) and the modulation fades after seven cycles. Fading of the charging capacity is due to trapping of intercalated Zn^{2+} in the NPs based on the XPS analysis that shows that a small amount of Zn^{2+} ions are retained in the film after the first charging cycle (Fig. S27). In addition, the chemisorption of Zn^{2+} on NPs at high pH may cause the precipitation of Zn^{2+} complexes that irreversibly aggregate and block the ion transport [36].

Incorporation of carbon nanotubes (CNTs) or Ag nanowires (NWs) to increase electrical conductivity of the multilayers and reduce the 'dead zones' trapping Zn^{2+} ions mitigates this problem. LBL films with an architecture of PAA/V_2O_3/CNT/PDDA (n=20) operated under the same conditions increased the total number of modulation cycles to 17 (Fig. S28, S29). In the end of the cycling, SEM images indicated an increase of the film cross-section and surface roughness (Fig. S30) associated with the entrapment of Zn^{2+} ions.

Replacement of CNTs with Ag NWs to form PAA/V_2O_3/AgNW/PDDA films (n=20) increases the total number of cycles before fading to 25 (**Fig. 4H-M,** S31). After the charging

WILEY-VCH

process of the first five cycles of V_2O_3/Ag NWs film, the peak at 852 nm in the *in-operando* CD spectrum nearly recovers to its initial intensity (**Fig. 4L-O,** S32). We also observed that these thin films exhibited higher polarization contrast due to high conductivity and potential plasmonic effects with Ag NWs. Enhanced CD amplitude for full charge-discharge cycle affords intercalation of smaller numbers of Zn^{2+} while retaining the optical fidelity of the cell to reduce entrapment. Voltage driven intercalation at ~50% of full capacity extends the polarization modulation for ~60 cycles for both *L-* and *D-*V_2O_3/Ag NWs films (**Fig. 4N, O**).

Conclusions: 'Built-in' chiral distortions in the lattice of V_2O_3 NPs induced by TA enantiomers on their surface result in concerted twist-untwist deformations upon ion-intercalations and related strong optical polarization effects. Similar cyclic reconfigurations of particle shapes are expected for multiple chiral nanostructures from metal oxides with a variety of optical, electrical, and magnetic properties. Considering the current voltage-driven polarization technologies based on liquid crystals, chiral ceramics offers extended temperature stability and spectral range, such as technologically relevant SWIR, NIR, and IR diapasons atypical for organic molecules. Variable solid-state chirality of V_2O_3 nanoparticles also offer a new materials platform for real-time chirality modulation and chiral photonics.

References

1. Hausbrand, R. *et al.* Fundamental degradation mechanisms of layered oxide Li-ion battery cathode materials: Methodology, insights and novel approaches. *Mater. Sci. Eng. B* **192**, 3–25 (2015).

2. Yeom, J. *et al.* Chiromagnetic nanoparticles and gels. *Science (80-.).* **359**, 309–314 (2018).

3. Knoppe, S. & Bürgi, T. Chirality in thiolate-protected gold clusters. *Acc. Chem. Res.* **47**, 1318–26 (2014).

4. Wang, P.-P., Yu, S.-J., Govorov, A. O. & Ouyang, M. Cooperative expression of atomic chirality in inorganic nanostructures. *Nat. Commun.* **8**, 14312 (2017).

5. Wang, Z. *et al.* Origami-Based Reconfigurable Metamaterials for Tunable Chirality. *Adv. Mater.* **29**, 1–7 (2017).

6. Choi, W. J. *et al.* Terahertz circular dichroism spectroscopy of biomaterials enabled by kirigami polarization modulators. *Nat. Mater.* **18**, (2019).

7. Kuzyk, A. *et al.* A light-driven three-dimensional plasmonic nanosystem that translates molecular motion into reversible chiroptical function. *Nat. Commun.* **7**, 10591 (2016).

8. Fernandez-Corbaton, I. *et al.* New Twists of 3D Chiral Metamaterials. *Adv. Mater.* **31**, 1807742 (2019).

9. Wang, S. *et al.* Guanosine Assembly Enabled Gold Nanorods with Dual Thermo-and Photoswitchable Plasmonic Chiroptical Activity. *ACS Nano* **14**, 6087–6096 (2020).

10. Gansel, J. K. *et al.* Gold helix photonic metamaterial as broadband circular polarizer. *Science* **325**, 1513–5 (2009).

11. Suo, Z. *et al.* Highly Chiroptical Detection with Gold–Silver Bimetallic Nanoclusters Circularly Polarized Luminescence Based on G-quartet Nanofiber Self-assembly. *J. Phys. Chem. C* **124**, 21094–21102 (2020).

12. Zhang, S. *et al.* Photoinduced handedness switching in terahertz chiral metamolecules. *Nat. Commun.* **3**, 942 (2012).

13. Wu, G. *et al.* Optical absorption edge evolution of vanadium pentoxide films during lithium intercalation. *Thin Solid Films* **485**, 284–289 (2005).

14. Zhang, W., Li, H., Al-Hussein, M. & Elezzabi, A. Y. Electrochromic Battery Displays with Energy Retrieval Functions Using Solution-Processable Colloidal Vanadium Oxide Nanoparticles. *Adv. Opt. Mater.* **8**, 1901224 (2020).

15. Mjejri, I., Rougier, A. & Gaudon, M. Low-Cost and Facile Synthesis of the Vanadium Oxides V2O3, VO2, and V2O5 and Their Magnetic, Thermochromic and Electrochromic Properties. *Inorg. Chem.* **56**, 1734–1741 (2017).

16. Zheng, J. *et al.* V2O3/C nanocomposites with interface defects for enhanced intercalation pseudocapacitance. *Electrochim. Acta* **318**, 635–643 (2019).

17. Marini, C. *et al.* Optical properties of V 1− x Cr x O 2 compounds under high pressure. *Phys.*

Rev. B **77**, 235111 (2008).

18. Heinz, H., Lin, T.-J., Kishore Mishra, R. & Emami, F. S. Thermodynamically Consistent Force Fields for the Assembly of Inorganic, Organic, and Biological Nanostructures: The INTERFACE Force Field. *Langmuir* **29**, 1754–1765 (2013).

19. Jung, S. H., Jeon, J., Kim, H., Jaworski, J. & Jung, J. H. Chiral arrangement of achiral Au nanoparticles by supramolecular assembly of helical nanofiber templates. *J. Am. Chem. Soc.* **136**, 6446–6452 (2014).

20. Dolamic, I., Varnholt, B. & Bürgi, T. Chirality transfer from gold nanocluster to adsorbate evidenced by vibrational circular dichroism. *Nat. Commun.* **6**, 7117 (2015).

21. Osipov, M. A., Pickup, B. T. & Dunmur, D. A. A new twist to molecular chirality: intrinsic chirality indices. *Molec. Phys.* **84**, 1193–1206 (1995).

22. Harris, A. B., Kamien, R. D. & Lubensky, T. C. Molecular chirality and chiral parameters. *Rev. Mod. Phys.* **71**, 1745–1757 (1999).

23. Kumar, P. *et al.* Photonically Active Bowtie Nanoassemblies with Chirality Continuum. *Res. Sq.* *[https//doi.org/10.21203/rs.3.rs-1614619/v1]* (2022).

24. Jiang, S. *et al.* Chiral ceramic nanoparticles and peptide catalysis. *J. Am. Chem. Soc.* **139**, 13701–13712 (2017).

25. Shelton, J. L. & Knowles, K. E. Thermally Activated Optical Absorption into Polaronic States in Hematite. *J. Phys. Chem. Lett.* **12**, 3343–3351 (2021).

26. Hao, C. *et al.* Chiral Semiconductor Nanoparticles for Protein Catalysis and Profiling. *Angew. Chemie - Int. Ed.* **58**, 7371–7374 (2019).

27. Yan, J. *et al.* Self-Assembly of Chiral Nanoparticles into Semiconductor Helices with Tunable near-Infrared Optical Activity. *Chem. Mater.* **32**, 476–488 (2020).

28. Ma, L., Cao, Y., Duan, Y., Han, L. & Che, S. Silver Films with Hierarchical Chirality. *Angew. Chemie Int. Ed.* **56**, 8657–8662 (2017).

29. Zhang, N. *et al.* Hydrated Layered Vanadium Oxide as a Highly Reversible Cathode for Rechargeable Aqueous Zinc Batteries. *Adv. Funct. Mater.* **29**, 1807331 (2019).

30. Kim, Y. *et al.* Reconfigurable chiroptical nanocomposites with chirality transfer from the macro-to the nanoscale. *Nat. Mater.* **15**, 461–468 (2016).

31. Probst, P. T. *et al.* Mechano-tunable chiral metasurfaces via colloidal assembly. *Nat. Mater.*

20, 1024–1028 (2021).

32. Li, Z. *et al.* Reversible plasmonic circular dichroism of Au nanorod and DNA assemblies. *J. Am. Chem. Soc.* **134**, 3322–3325 (2012).

33. Wang, Y., Zhang, Y.-M. & Zhang, S. X.-A. Stimuli-Induced Reversible Proton Transfer for Stimuli-Responsive Materials and Devices. *Acc. Chem. Res.* **54**, 2216–2226 (2021).

34. Ariga, K., Hill, J. P. & Ji, Q. Layer-by-layer assembly as a versatile bottom-up nanofabrication technique for exploratory research and realistic application. *Phys. Chem. Chem. Phys.* **9**, 2319 (2007).

35. Zhao, S. *et al.* The Future of Layer-by-Layer Assembly: A Tribute to ACS Nano Associate Editor Helmuth Mohwald. *ACS Nano* **13**, (2019).

36. Yang, G., Li, Q., Ma, K., Hong, C. & Wang, C. The degradation mechanism of vanadium oxide-based aqueous zinc-ion batteries. *J. Mater. Chem. A* **8**, 8084–8095 (2020).

37. Shimazaki, Y., Mitsuishi, M., Ito, S. & Yamamoto, M. Preparation of the layer-by-layer deposited ultrathin film based on the charge-transfer interaction. *Langmuir* **13**, 1385–1387 (1997).

38. Yang, S. *et al.* Water uptake behavior of hydrogen-bonded PVPON–PAA LBL film. *Soft Matter* **2**, 699–704 (2006).

39. Shim, B. S. *et al.* Integration of conductivity, transparency, and mechanical strength into highly homogeneous layer-by-layer composites of single-walled carbon nanotubes for optoelectronics. *Chem. Mater.* **19**, 5467–5474 (2007).

40. Shim, B. S., Zhu, J., Jan, E., Critchley, K. & Kotov, N. A. Transparent conductors from layer-by-layer assembled SWNT films: importance of mechanical properties and a new figure of merit. *ACS Nano* **4**, 3725–34 (2010).

41. Cheng, G., Di, J. & Wang, Y. Chiroptical Study of Metal@ semiconductor–Molecule Composites: Interaction between Cysteine and Ag@ Ag3PO4 Core–Shell Hybrid Nanorods. *J. Phys. Chem. C* **119**, 22122–22130 (2015).

42. Jiu, J. *et al.* Facile synthesis of very-long silver nanowires for transparent electrodes. *J. Mater. Chem. A* **2**, 6326–6330 (2014).

43. Vanommeslaeghe, K., Raman, E. P. & MacKerell Jr, A. D. Automation of the CHARMM General Force Field (CGenFF) II: assignment of bonded parameters and partial atomic charges. *J. Chem. Inf. Model.* **52**, 3155–3168 (2012).

44.   Vanommeslaeghe, K. *et al.* CHARMM general force field: A force field for drug-like molecules compatible with the CHARMM all-atom additive biological force fields. *J. Comput. Chem.* **31**, 671–90 (2010).

45.   Crans, D. C. & Tracey, A. S. The Chemistry of Vanadium in Aqueous and Nonaqueous Solution. in *Vanadium Compounds* 2–29 (ACS Publications, 1998). doi:10.1021/bk-1998-0711.ch001.

46.   Emami, F. S. *et al.* Force Field and a Surface Model Database for Silica to Simulate Interfacial Properties in Atomic Resolution. *Chem. Mater.* **26**, 2647–2658 (2014).

47.   Banerjee, R., Mohanty, A., Chakravarty, S., Chakladar, S. & Biswas, P. A single-step process to leach out rare earth elements from coal ash using organic carboxylic acids. *Hydrometallurgy* **201**, 105575 (2021).

48.   Mishra, R. K., Kanhaiya, K., Winetrout, J. J., Flatt, R. J. & Heinz, H. Force field for calcium sulfate minerals to predict structural, hydration, and interfacial properties. *Cem. Concr. Res.* **139**, 106262 (2021).

49.   Phillips, J. C. *et al.* Scalable molecular dynamics with NAMD. *J. Comput. Chem.* **26**, 1781–802 (2005).

50.   Gowers, R. J. *et al. MDAnalysis: a Python package for the rapid analysis of molecular dynamics simulations*. (2019).

51.   Michaud-Agrawal, N., Denning, E. J., Woolf, T. B. & Beckstein, O. MDAnalysis: a toolkit for the analysis of molecular dynamics simulations. *J. Comput. Chem.* **32**, 2319–2327 (2011).

52.   Choi, J.-H. & Cho, M. Direct Calculations of Mid- and Near-IR Absorption and Circular Dichroism Spectra of Chiral Molecules Using QM/MM Molecular Dynamics Simulation Method. *J. Chem. Theory Comput.* **7**, 4097–4103 (2011).

53.   Millar, G., Weinberg, N. & Mislow, K. On the Osipov–Pickup–Dunmur chirality index: why pseudoscalar functions are generally unsuitable to quantify chirality. *Mol. Phys.* **103**, 2769–2772 (2005).

54.   Cha, M. *et al.* Unifying structural descriptors for biological and bioinspired nanoscale complexes. *Nat. Comput. Sci.* **2**, 243–252 (2022).

55.   Ramírez, A. *et al.* Evaluation of MnO x, Mn2O3, and Mn3O4 electrodeposited films for the oxygen evolution reaction of water. *J. Phys. Chem. C* **118**, 14073–14081 (2014).

56.   Mei, Y., Zhou, Z. & Luo, H. L. Electrical resistivity of rf-sputtered iron oxide thin films. *J. Appl. Phys.* **61**, 4388–4389 (1987).

57.   Roy, T. K., Sanyal, D., Bhowmick, D. & Chakrabarti, A. Temperature dependent resistivity study on zinc oxide and the role of defects. *Mater. Sci. Semicond. Process.* **16**, 332–336 (2013).

58.   Kandalkar, S. G., Gunjakar, J. L., Lokhande, C. D. & Joo, O.-S. Synthesis of cobalt oxide interconnected flacks and nano-worms structures using low temperature chemical bath deposition. *J. Alloys Compd.* **478**, 594–598 (2009).

59.   Jiang, H. *et al.* Ultrafine V2O3 nanowire embedded in carbon hybrids with enhanced lithium storage capability. *Ind. Eng. Chem. Res.* **54**, 2960–2965 (2015).

60.   Kusano, E., Theil, J. A. & Thornton, J. A. Deposition of vanadium oxide films by direct-current magnetron reactive sputtering. *J. Vac. Sci. Technol. A Vacuum, Surfaces, Film.* **6**, 1663–1667 (1988).

61.   Sarrigiannidis, S. O. *et al.* Chiral Tartaric Acid Improves Fracture Toughness of Bioactive Brushite–Collagen Bone Cements. *ACS Appl. Bio Mater.* **3**, 5056–5066 (2020).

62.   Fu, B. *et al.* Interfacial interaction of tartaric acid with hydroxyapatite and enamel. *J. Mater. Sci. Mater. Med.* **16**, 827–831 (2005).

63.   Gautier, C. & Bürgi, T. Chiral inversion of gold nanoparticles. *J. Am. Chem. Soc.* **130**, 7077–7084 (2008).

64.   Rodríguez-Zamora, P. *et al.* Effect of the Metal–Ligand Interface on the Chiroptical Activity of Cysteine-Protected Nanoparticles. *Small* 2004288 (2021).

65.   Tohgha, U. *et al.* Ligand induced circular dichroism and circularly polarized luminescence in CdSe quantum dots. *ACS Nano* **7**, 11094–102 (2013).

66.   Moloney, M. P., Gun'ko, Y. K. & Kelly, J. M. Chiral highly luminescent CdS quantum dots. *Chem. Commun.* **7345**, 3900 (2007).

67.   Li, Y. *et al.* Tunable Chiroptical Properties from the Plasmonic Band to Metal–Ligand Charge Transfer Band of Cysteine-Capped Molybdenum Oxide Nanoparticles. *Angew. Chemie Int. Ed.* **57**, 10236–10240 (2018).

68.   Cheng, J. *et al.* GoldHelix: Gold Nanoparticles Forming 3D Helical Superstructures with Controlled Morphology and Strong Chiroptical Property. *ACS Nano* **11**, 3806–3818 (2017).

69.   Yeom, J. *et al.* Chiral supraparticles for controllable nanomedicine. *Adv. Mater.* **32**, 1903878 (2020).

Author contributions: X.S. carried out most experimental work in this study. C.Z and H.H. carried out MD simulations using Interface Force Field. M.C. developed a code and calculated wOPD. Y.W. assistant for the synthesis and carry out the XRD measurement during revision. P.K. carried out VCD, ROA and interpreted multiple functions. J.L. carried out electrodynamic calculations. Y.L. created initial set of data. Y.C assisted with electrochemical measurements. X.M. calculated the geometrical mechanical models of the twist-untwist deformations.

Competing interests: N.A.K is a founder of a company *Photon Semantics, LLC* working on machine vision with chiral particles.

Data and materials availability: All data, code, and materials used in the analysis must be available in some form to any researcher for purposes of reproducing or extending the analysis. Include a note explaining any restrictions on materials, such as materials transfer agreements (MTAs). Note accession numbers to any data relating to the paper and deposited in a public database; include a brief description of the data set or model with the number. If all data are in the paper and supplementary materials, include the sentence "All data are available in the main text or the supplementary materials."
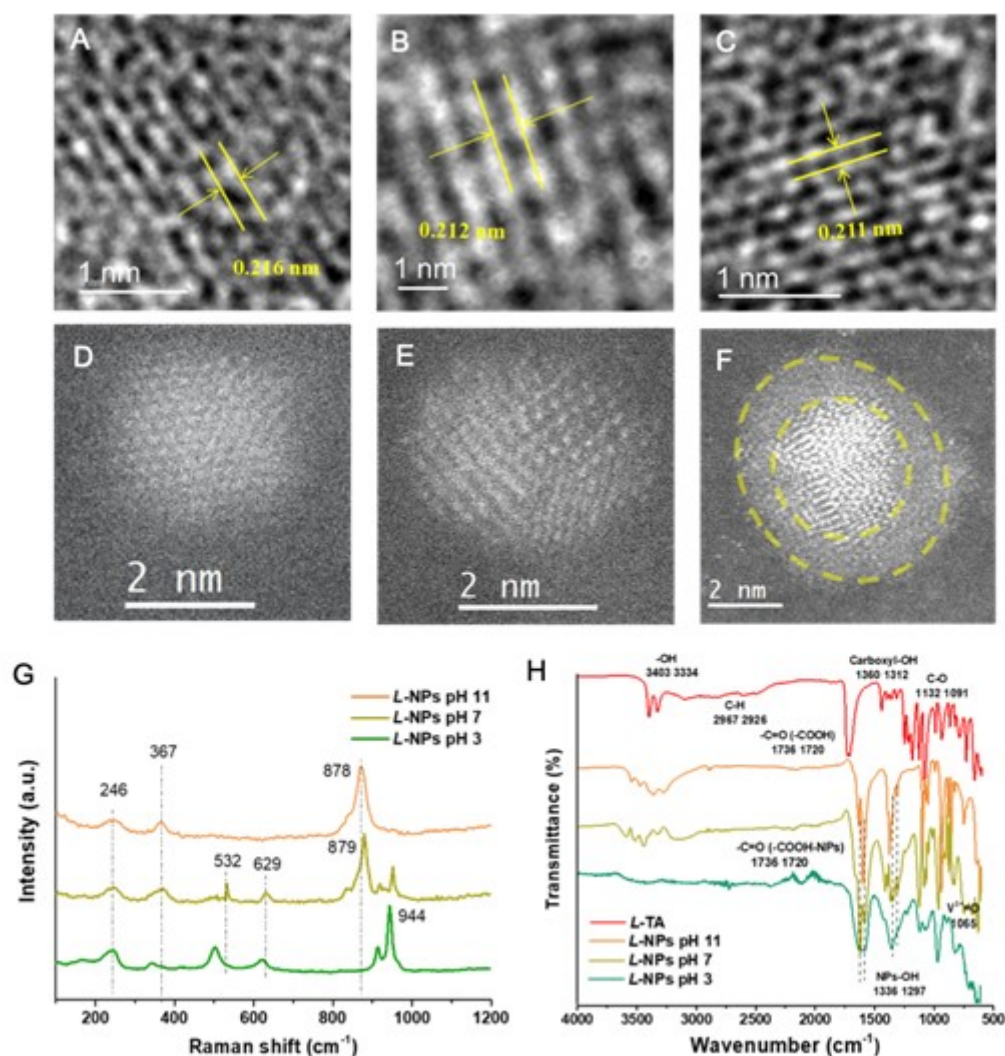
Supplementary Materials

Materials and Methods
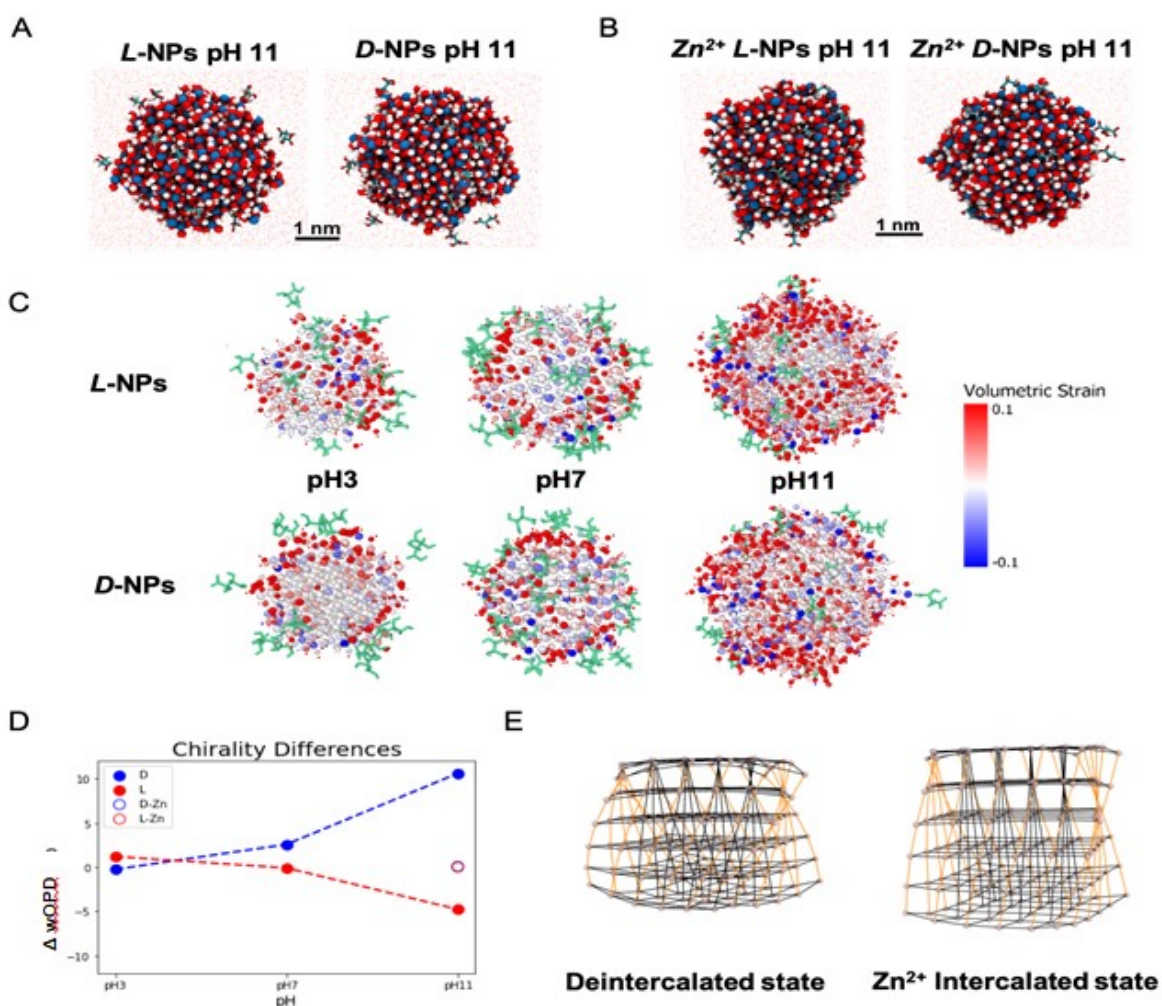
Figs. S1 to S32

Tables S1 to S6

Figures

Figure 1. Structural characterization of chiral V₂O₃ NPs. (A-C) HRTEM images of *L*-NPs obtained at (A) pH 3, (B) pH 7, (C) pH 11. (**D-F**) STEM images of *L*-NPs at (D) pH 3, (E) pH 7, (F) pH 11. The yellow dashed lines in (F) denote the interfacial and core regions of the NP. (**G**) Raman and (**H**) FTIR spectra of V₂O₃ *L*-NPs at pH 3, 7, 11.

Figure 2. Computational modeling of atomic geometries of chiral V₂O₃ nanoparticles with and without Zn²⁺ intercalation. (**A**) The typical atomistic structures of equilibrated NPs at pH 11 in water. (**B**) The typical atomistic structures of equilibrated Zn²⁺ intercalated NPs at pH 11. Zn²⁺ ratio is 10% in the core part. (**C**) Calculated volumetric strain of TA modified NPs with reference to bare NPs. The color bar shows the range of the volumetric strain. The green molecules are TA molecules. (**D**) The wOPD values of *L/D*-NPs at different pH (solid circle) and the values of Zn²⁺ intercalated *L/D*-NPs pH 11 (circle). (**E**) Geometrical mechanical models of NPs and Zn²⁺ intercalated NPs which expanded while untwisting. Orange bonds depict intrinsic chiral strain lines from the TA molecules attached to NP surfaces.
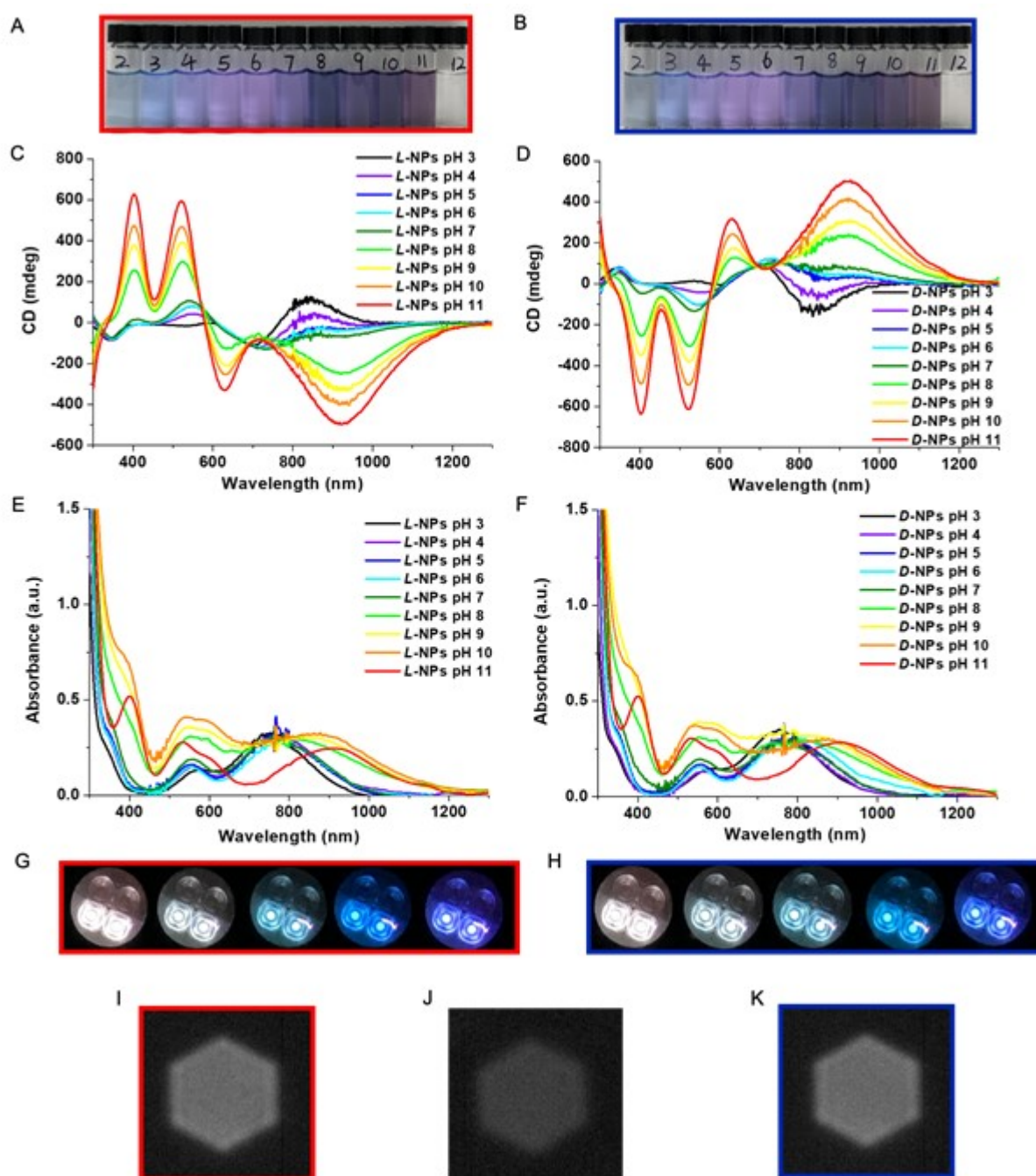
Figure 3. Circular polarization effects for dispersions and thin films. (**A** and **B**) Photographs of NP solutions made with *L*- and *D*-TA NPs at pH 2 to 12. (**C** and **D**) CD (**E** and **F**) UV-Vis-NIR absorbance of *L*- and *D*-NPs at pH 3 to 11. (**G** and **H**) Photographs of light transmitted through dispersions of *L*- and *D*-V$_2$O$_3$ NPs at pH 11; fixed *Polarizer 1* and clockwise (G for *L*-TA-NPs) and counterclockwise (H for *D*-TA-NPs) rotation of *Polarizer 2* (each color changed with rotation of ~3 degrees; see Fig. S18 for polarization experiment schematics). Photographs of (**I**) *L*-, (**J**) *rac-,* and (**K**) *D*-V$_2$O$_3$ NPs dispersions at

pH 11 in a cross-polarizer setup. Transmitting NIR light with a wavelength of 360-2400 nm with detector sensitive to wavelengths of ~1000 nm.
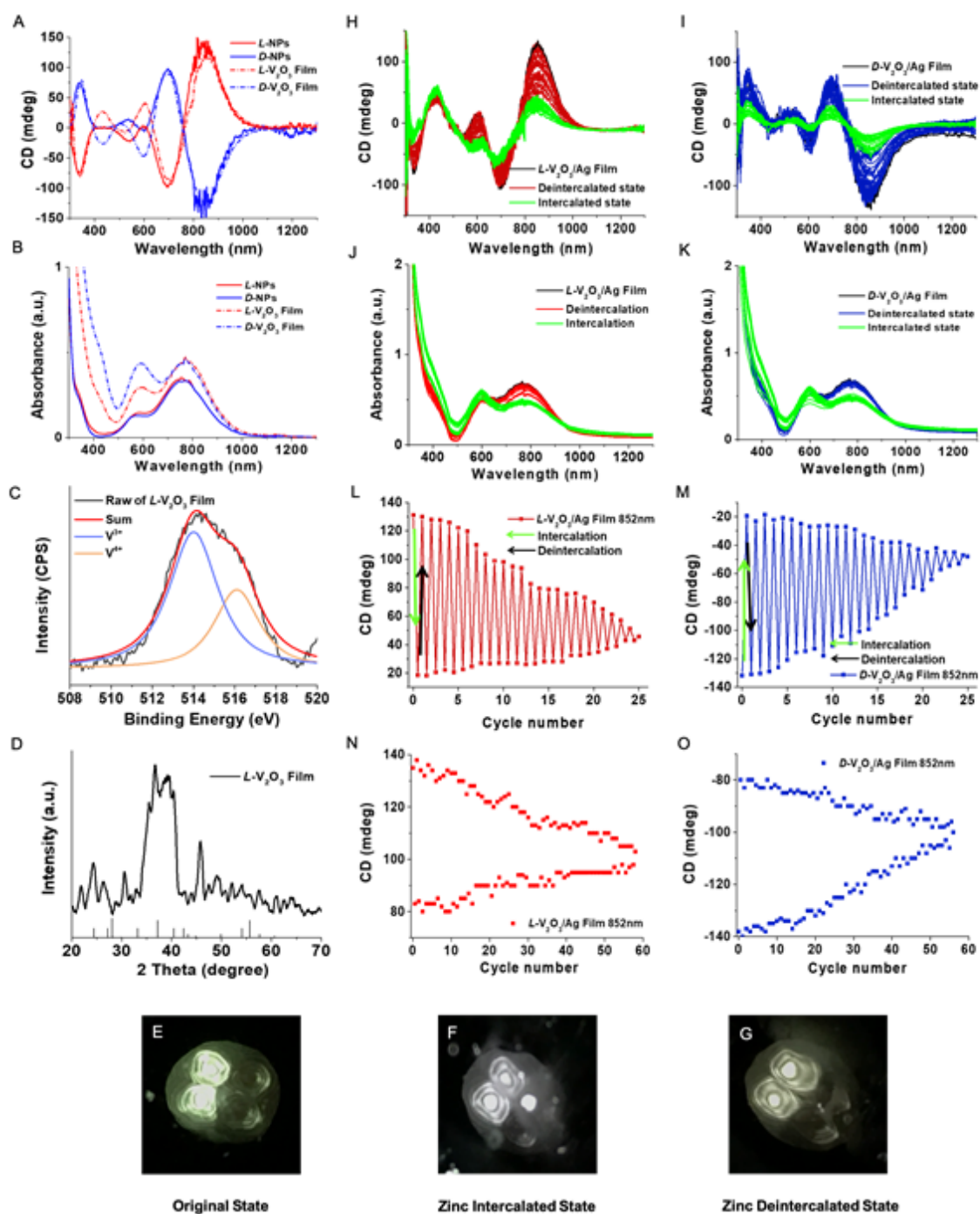
Figure 4. **Cyclic behavior of circularly polarizing thin films from chiral nanoparticles.** (**A**) CD and (**B**) absorbance of *L*- and *D*- NP solutions (in H$_2$O, solid line) and *L*-NP film (on ITO-glass, dashed line). (**C**) XPS and (**D**) XRD of *L*-V$_2$O$_3$ film. Compare with the XRD pattern for NP powders in Fig. S4C.

Photographs of light transmitting through the *L*-NPs film in (**E**) original state, (**F**) after zinc intercalation, (**G**) after zinc deintercalation. (**H** and **I**) CD and (**J** and **K**) absorbance of *L*- and *D*-V$_2$O$_3$/Ag NWs films. (**L-O**) Cycling performance of the films monitored as CD intensity of films at 852 nm after cycles of zinc ions intercalation and deintercalation.

Table of Contents (ToC) Text :

Chiral V$_2$O$_3$ nanoparticles display rich palette of intense chiroptical bands. Intercalation of Zn^{2+} leads to untwist deformation and modulation of optical activity, which is remarkably strong for IR and NIR range because V$_2$O$_3$ nanoparticles have g-factors ~100-400 times higher than other nanostructures. Device prototypes based on layer-by-layer assembled nanocomposite films provide a pathway to versatile voltage-driven photonic devices.